Egypt. J. Chem. **Vol. 68**, No. 11 pp. 497-515 (2025)

Egyptian Journal of Chemistry

http://ejchem.journals.ekb.eg/

Photoactive Folic acid nanocomposite for targeted PDT of Breast and Liver Cancer cell lines

Ahmed Allam[1], Walid Tawfik[1*], Mahmoud T. Abo-Elfadl[2,3] , Ahmed M Fahmy[4] ,Souad A Elfeky[1]

[1]*National Institute of Laser Enhanced Sciences, LAMPA Department, Cairo University, Cairo 12613, Egypt.*

[2] *Biochemistry Department, Biotechnology Research Institute, National Research Centre, Cairo 12622, Egypt.*

[3] *Cancer Biology and Genetics Laboratory, Centre of Excellence for Advanced Sciences, National Research Centre, Cairo 12622, Egypt.*

[4]*Pathology Department., National Cancer Institute, Cairo University, Cairo 12613, Egypt*.

Abstract

Cancer is a pervasive global health challenge, with breast and liver cancers being at the forefront. A novel treatment approach involves using chitosan nanocarriers and the photosensitizing agent pheophorbide-a to selectively target and eradicate cancer cells through folic acid (FO)-guided laser activation. Building on our prior breakthroughs in photothermal therapy (PTT) using gold nanorods, this study synthesizes and characterizes Pheophorbide-a@Chitosan-folic acid nanocomposites (Pha@CH-FO NC) for targeted photodynamic therapy (PDT). Results demonstrate synergistic ROS-mediated cytotoxicity in breast and liver cancer cells (IC50: 122.74 µg/mL for MCF7), with apoptosis confirmed via Bcl-2 downregulation (60–70%, $p < 0.001$). This dual-modal approach, integrating PDT with PTT insights, advances precision oncology. The synthesized Pheophorbide-a@Chitosan nanoparticles conjugated with folic acid (Pha@CH-FO NC) underwent thorough characterization by FTIR, TEM, UV-VIS, and HPLC analyses. Results from MTT assays showed that Pha@CH-FO NC had modest cytotoxicity profiles, with IC_{50} values of 122.74 µg/mL for MCF7 and 217.27 µg/mL for T-47D. There were no discernible IC_{50} values for MDA-MB-231 and HepG2 cell lines after a 24-hour incubation period. Moreover, when MCF7 and T-47D cells were exposed to half the IC_{50} of Pha@CH-FO NC combined with laser irradiation (405 nm, 50 mW/96 seconds), they exhibited 50% cytotoxicity. MDA-MB-231 and HepG2 cells showed comparable effects under 10 mW/500 seconds of laser irradiation. Apoptosis was the predominant mode of cell death in all treated cell lines, as evidenced by decreased Bcl-2 gene expression (an apoptosis-suppressing gene) in treated cell lines compared to controls. Additionally, increased production of reactive oxygen species (ROS) was observed in irradiated MCF7 and T-47D cells at 50 mW/96 seconds, MDA-MB-231 cells at 50 mW/200 seconds, and HepG2 cells at 10 mW/1000 seconds. This study highlights the potential of Pha@CH-FO NC in enhancing PDT effectiveness and inhibiting cancer progression, making it a crucial component in targeted cancer therapies. The evaluation of various photodynamic approaches underscores the potential of this novel photoactive NC system in advancing PDT and cancer treatment paradigms.

Keywords: Photodynamic Therapy (PDT), Folic Acid-Conjugated, Nanocomposite. Breast Cancer Treatment, Liver Cancer Treatment, Chitosan Nanoparticles, Pheophorbide-a, Reactive Oxygen Species (ROS).

Introduction:

Cancer continues to pose a significant global health challenge, with breast and liver cancers being among the most prevalent and life-threatening malignancies[1, 2]. Photodynamic therapy (PDT) has emerged as a promising treatment modality for various types of cancer, utilizing photosensitizing agents to target and destroy cancer cells selectively upon light activation[3]. However, the effectiveness of PDT can be limited by factors such as poor solubility and bioavailability of the photosensitizer, as well as non-specific tissue distribution [4]. In recent years, chitosan nanoparticles (CH NPs) have garnered attention as a versatile drug delivery system due to their biocompatibility, biodegradability, and ability to encapsulate a wide range of therapeutic compounds. Chitosan, a natural polysaccharide, has potent anticancer activity through various mechanisms, including cell cycle disruption, interference with DNA, RNA, and protein synthesis and inhibition of cancer cell growth [5]. Studies have demonstrated that chitosan oligosaccharide inhibits the growth of hepatoma cells and induces apoptosis, possibly through the downregulation of Bcl-2 and upregulation of Caspase-3 [6]. Similarly, chitosan inhibits the proliferation of breast cancer cells, leading to apoptosis and S-phase

*Corresponding author e-mail : walid_tawfik@niles.edu.eg ; (Walid Tawfik)

Receive Date: 08 February 2025, Revise Date: 24 March 2025, Accept Date: 08 April 2025

DOI: 10.21608/ejchem.2025.358951.11281

cell cycle arrest, potentially through its interaction with DNA [7]. Furthermore, shrimp-derived chitosan has antiproliferative and cytotoxic effects on both hepatic and breast cancer cells, with alterations in the cell cycle profile and the expression of pro- and anti-apoptotic genes [8]. These findings indicate that chitosan's anticancer effects are mediated through a combination of apoptosis induction, cell cycle arrest, and alterations in gene expression. FO can be conjugated with anticancer drugs to target cancer cells that overexpress folate receptors, allowing for more targeted drug delivery and potentially reducing side effects on healthy tissues [9]. FO has a chemo-preventive effect on hepatocellular carcinoma (HCC) by inhibiting the expression of LCN_2 through the promotion of histone H_3 lysine 9 di-methylation ($H_3K_9Me_2$) in the LCN_2 promoter [10]. In addition, FO is crucial for DNA synthesis and repair through the methylation process. Cancer cells often exhibit abnormal DNA methylation patterns, and FO can regulate these processes by providing one-carbon units necessary for methylation reactions [11]. FO analogs such as methotrexate are commonly used as antimetabolites in cancer treatment. These compounds interfere with the production of nucleotides needed for DNA synthesis, leading to cancer cell death. In breast cancer cells, FO induces apoptosis by targeting the PTEN/AKT/P53 signaling pathway [12]. This is further supported by using FO in folate receptor-targeted immunotherapy, which enhances the immune response against cancer cells [13]. Thus, FO may have a dual mechanism of action in targeting hepatic and breast cancer cells, involving both direct cytotoxic effects and immune modulation. Pheophorbide-a, a chlorophyll derivative, has shown promise in PDT for breast cancer. Pheophorbide-a absorbs light most strongly at these two specific wavelengths, one in the UV range around 337 nm and the other in the red region around 667 nm [14]. Studies have demonstrated its ability to induce apoptosis in breast cancer cells [15, 16]. It has also been found to efficiently cleave DNA, suggesting a potential role in PDT for cancer [17]. Further research on pheophorbide-a derivatives has shown that modifications can enhance their photophysical properties and photodynamic tumoricidal effects [18]. Hence, pheophorbide-a and its derivatives have the potential in PDT for liver and breast cancer. The use of chitosan as a nanocarrier for targeted photodynamic therapy (PDT) in breast and hepatic cancer cell lines has been explored in several studies. Sahu et al. 2010 demonstrated the potential of CH-based NPs for targeted drug delivery, showing that folate enhanced cellular uptake of NPs and apoptosis in cancer cells (HeLa and B16F1). Wu and Zhao 2016)further enhanced the efficacy of CH/FO by incorporating pyro-pheophorbide as a photosensitizer, resulting in strong phototoxicity (approximately 60%–74%) against HeLa cells, suggesting good biocompatibility and anticancer efficacy. Aibani et al. 2021)also confirmed the effectiveness of CH/FO as an efficient target gene carrier for SKOV3 and MCF-7 tumor cells that express the folate receptor. These studies collectively support the potential of chitosan nanocarriers for targeted PDT in breast and hepatic cancer cell lines, particularly when combined with folic acid as a targeting molecule. Cytotoxicity in Pha@CH-FO NC-treated cells correlated with ROS overproduction (3–5-fold increase, $p < 0.001$), mirroring findings in AuNRs-PTT models where ROS triggered caspase-3 activation [2]. Notably, apoptosis dominated (65% via AO/EtBr) over necrosis (<5%), contrasting with PTT's thermal effects [1], thus validating PDT's precision. This aligns with our earlier observation that folate receptor targeting enhances nanocarrier uptake in mammary tumors [2]. This work aims to explore the potential use of pha@CH-FO NC in the context of breast and liver cancer PDT(in vitro). By coating CH NPs (carrier) with Pha, (a potent photosensitizer), and FO, (which can enhance specific cellular uptake through folate receptor targeting), a novel nanocarrier system for targeted cancer PDT can be developed.

Materials and methods

Chemicals

Folic acid, anhydrous diethyl ether, acetone and triethylamine were purchased from SD Fine-Chem Limited Company (India). Dimethyl sulfoxide (DMSO), and sodium hydroxide pellets (98%) were obtained from Advent Chembio PVT Limited Company (India). Pheophorbide-a powder sodium tripolyphosphate (TPP), dicyclohexylcarbodiimide (DCC), hydrochloric acid (HCl), and N-Hydroxysuccinimide (NHS) were purchased from Sigma Aldrich (U.S.A). Chitosan powder was acquired from Alpha Chemika (India). Sodium monochloroacetate was obtained from Loba Chemie Pvt Limited (India). Acetic acid was purchased from El Nasr Pharmaceutical Co. (Egypt).

Preparation of chitosan in an acetate buffer

An acetate buffer was prepared by dissolving 5.772 g of sodium monoacetate in 800 mL of distilled water. Next, 1.778 g of acetic acid was added, and the solution's pH was adjusted to 5.0 using 10 mL hydrochloric acid (HCl). Finally, distilled water was added to reach a total volume of 1 liter [22]. Subsequently, chitosan powder was introduced into the acetate buffer at 1 g per 100 mL.

Preparation of CH-FO solution

In the first step, a solution of CH-FO was prepared by adding 450 mg of folic acid to 10 mL of dimethyl sulfoxide (DMSO), followed by the addition of 93 mg of Dicyclohexylcarbodiimide (DCC), 77 mg of N-Hydroxysuccinimide (NHS), and 0.5 mL of Triethylamine. The mixture was stirred overnight at 30°C. Subsequently, centrifugation at 10,000 rpm was performed using a Sigma 3-18k centrifuge to remove dicyclohexyl urea byproducts. The resulting solution was then slowly added as a drip into anhydrous diethyl ether containing 30% acetone, followed by centrifugation at 1,000 rpm to separate the yellow precipitate. The precipitate was washed several times with anhydrous diethyl ether. The NHS-ester of folic acid in DMSO solution was then added to the prepared chitosan in acetate buffer (pH=5.5) and the mixture was stirred at room temperature for 10 hours in the dark. The pH of the mixture was adjusted to 9 using 10 M NaOH dropwise, followed by centrifugation at 10,000 rpm to obtain a precipitate, which was washed with distilled water multiple times and finally dissolved in a 2% acetic acid aqueous solution. Freeze-drying was then carried out to obtain CH-FO (Li et al. 2017).

The obtained mixture was divided into two portions to prepare a) CH-FO NC and b) Pha@CH-FO NC.

a) Preparation of CH-FO nanoconjugate (CH-FO NC)

To prepare FC-NPs, 42 mg of CH-FO was dissolved in 21 mL of 2% acetic acid in an aqueous solution to achieve a final concentration of 2 mg/ml. The solution was then adjusted to pH=5.5 using 10 M NaOH. Another solution of CH-FO was prepared at a concentration of 4 mg/mL in 1.5 mL of 2% acetic acid and adjusted to pH=5 using 10 M NaOH. Subsequently, 0.5 mL of a 2 mg/mL tripolyphosphate (TPP) solution was slowly added dropwise during magnetic stirring and further stirred for 30 minutes to convert CH-FO solution into CH-FO NC (Li et al. 2017).

b) Preparation of Pha@CH-FO NC

To prepare Pha@CH-FO NC, CH-FO was prepared in a 2% acetic acid aqueous solution at 2 mg/mL concentration in 3 mL of solution. Pheophorbide (2025 mg) was added to the solution, which was then adjusted to pH=5.5 using 10 M NaOH and stirred at room temperature for 24 hours in the dark to obtain Pha@CH-FO. The resulting Pha@CH-FO was dissolved in a 2% acetic acid aqueous solution to achieve a final 4 mg/mL concentration and adjusted to pH=5 using 10 M NaOH. Subsequently, 0.5 mL of a 2 mg/mL TPP solution was slowly added dropwise during magnetic stirring and further stirred for 30 minutes to obtain Pha@CH-FO NC (Li et al. 2017).

Characterization

A JEOL2010F transmission electron microscope (JEOL, Germany) with a field-emission gun running at 120 kV performed TEM imaging of Pha@CH-FO NC. On an amorphous carbon–copper grid, a drop of a very diluted sample solution was placed and allowed to evaporate at room temperature. Absorption spectra were captured by UV-VIS spectrophotometer DS5 (200-1100 nm) from Edinburgh instruments UK. Fourier transform infrared (FTIR) spectroscopy (4000-500 cm^{-1}) was accomplished using a Bruker Vertex 80, Bruker, USA. Zeta potential nano (Malvern, UK) was utilized to calculate the NC charges of Pha@CH-FO NC. HPLC Chromatograph was done by YL-9100 system with C-18 (250 mm × 4.6 mm × 5µm). The mobile phase used was acetonitrile and methanol in the ratio 40:60 at a 1 mL/min flow rate. Wavelength was fixed at 350 nm. Analysis was performed at the Micro Analytical Center, Cairo University, Giza Governorate, Egypt

Cell lines and cell culture

The human epithelial hepatocellular carcinoma cell line, HepG2, the human epithelial breast adenocarcinoma cell line, MCF7, the human epithelial breast mammary gland ductal carcinoma cell line, T-47D, and the human epithelial breast triple negative mammary gland adenocarcinoma, cell line, MDA-MB-231, were all purchased from the American Type Cell Culture (ATCC, USA). All cell lines were routinely cultured in DMEM high glucose medium. The medium consists of 10% fetal bovine serum (FBS), 2 mM L-glutamine, and 1% antibiotic-antimycotic cocktail, all from Lonza, (Basel, Switzerland). Cells were maintained at sub-confluency at 37ºC in humidified air containing 5% CO2. For sub-culturing, monolayer cells were harvested after trypsin/EDTA treatment at 37°C. Cells were used when confluence reached 75% [25].

Cytotoxic assay (MTT)

Using the MTT assay, the cytotoxicity of the samples was screened on all cell lines under different conditions: without Laser for 24 and 48 hrs. time interval at serial dilution ranging from 100 µg/mL to 3.125 µg/mL to determine the optimum IC_{50} and time interval for each sample. With laser (405 nm, DIODE cnilaser MLL-III-405) application on the chlorophyll sample at half its IC_{50} but at different laser conditions (50 mW at 24, 48, 100, 200, 400, and 800 seconds-25 mW at 48, 100, 200, 400, 800, and 1600 seconds-10 mW at 250, 500, 1000, and 2000 seconds). After 24 hrs. of sample and laser application, MTT was added for 4 hrs. and the formazan crystals were solubilized using 180 µL of acidified isopropanol/well. The optical density was measured at 570 nm according to [26] using a microplate ELISA reader (FLUOstar OPTIMA, BMG LABTECH GmbH, Ortenberg, Germany). Four repeats were performed for each laser application and the average was calculated. The formula used to calculate the cytotoxicity was as follows:

Percentage of relative viability = (OD of sample) / (OD of control) X 100 [27]

Mode of cell death detection

Using the fluorescing staining technique to detect the mode of cell death, cells were cultured on 8 well cell culture slides (SPL, Seoul, South Korea) at a density of 104 cells/well. The samples were adjusted to a final concentration of half IC_{50} of the sample on its respective cell line. After applying the optimum laser conditions, the cells were incubated for 24 hrs. and the mode of the cell death was investigated by staining with acridine orange (100 µg/mL) and ethidium bromide (100 µg/mL) dual stain dissolved in phosphate buffer saline (PBS) at equal volumes (El-ghannam et al. 2024), all obtained from Merck KGaA (Darmstadt, Germany). The cells were stained and investigated under the fluorescent microscope (AxioImager Z2, Zeiss, Jena, Germany). Cells with green color were considered live cells, while those with yellow, orange, or red colors were classified as early apoptotic, late apoptotic, or necrotic cells, respectively [29]. Experiments were repeated three times.

Bcl-2 protein expression detection

The cells were cultured on 8-well cell culture slides (SPL, Seoul, South Korea) at a density of 10^4 cells/well, and the respective ½ IC_{50} of the Pha@CH-FO NC sample was added to each cell line. The cells were irradiated with the Laser using the optimum laser conditions obtained from the cytotoxicity test. After that, the cells were fixed with 4% paraformaldehyde and permeabilized with

0.1% TritonX-100. The cells were then blocked with 1% bovine serum albumin and incubated overnight at 4ºC with the anti-Bcl-2 antibody ab59348 (Abcam, Cambridge, United Kingdom) at a dilution of 1/500 (Wang, 1998). After extensive washing, the cells were incubated with the secondary antibody goat anti rabbit IgG (Alexa Fluor®488) ab150077 (Abcam, Cambridge, United Kingdom) at a dilution of 1/1000. After washing and air drying, the glycerol mounting medium with DAPI (ab188804, Abcam, Cambridge, United Kingdom) was used as an anti-fade and counterstain for the nucleus. The cells were then visualized under the fluorescent microscope AxioImager Z2 (Zeiss, Jena, Germany) and the fluorescence intensity was measured using Zen11 Blue edition software (Zeiss, Jena, Germany).

ROS detection

Each cell line was cultured in a black cell culture 96-well plate at a density of $5*10^4$ cells/well with the following format: 4 wells for the 50-mW laser/ 96 seconds (for MCF7, T-47D, and HepG2 cell lines) and 200 seconds for the MDA-MB-231 cell line. 4 wells for the 25-mW laser/ 400 seconds for the four cell lines. There were 4 wells for the 10-mW laser/ 500 seconds (for MDA-MB-231 and HepG2 cell lines) and 1000 seconds (for MCF7 and T-47D cell lines). 4 wells of cells with samples only without Laser, 4 wells of positive control detector, 4 wells of negative control cells. Using the ROS Fluorometric Assay Kit, Elabscience, E-BC-K138-F (Texas, USA), the intensity of the ROS fluorescent detector was measured by the microplate ELISA reader (FLUOstar OPTIMA, BMG LABTECH GmbH, Ortenberg, Germany) at Ex/Em 500/525 nm [31].

Statistics

Data are presented as mean ± SD. The dose-response curve was calculated using non-linear regression analysis with 5 parametric logistic curve equations. Ordinary One-Way ANOVA was used for multiple group comparisons using GraphPad Prism 9.4.1 (458) for MacOS, GraphPad Software (San Diego, California USA, www.graphpad.com).

Results and discussion

Characterization of the NPs

FTIR provides valuable insights into composite materials' structural changes and chemical bonding. Typical peaks observed in the FTIR spectrum of chitosan NPs are shown in Fig. 1. The wider peak observed at 3440 cm^{-1} suggests the presence of stretching vibrations associated with O-H and N-H functional groups [32]. The N-O-P peak at 1535 cm^{-1} suggests the presence of nitrogen, oxygen, and phosphorus in the sample. Additionally, the carbonyl stretching vibration is observed at 1580 cm^{-1}, indicating the existence of carbonyl groups within the chitosan structure. A peak at 1630 cm^{-1} signifies the –NH bending vibration, which provides further information about the molecular conformation and bonding arrangement of chitosan NPs [33]. Peaks corresponding to the asymmetrical and symmetrical stretching of -CH_2- were identified at 2920 and 2850 cm^{-1}, respectively. The asymmetrical and symmetrical bending vibrations of -CH_3 were detected at 1470 and 1380 cm^{-1}, respectively [34].

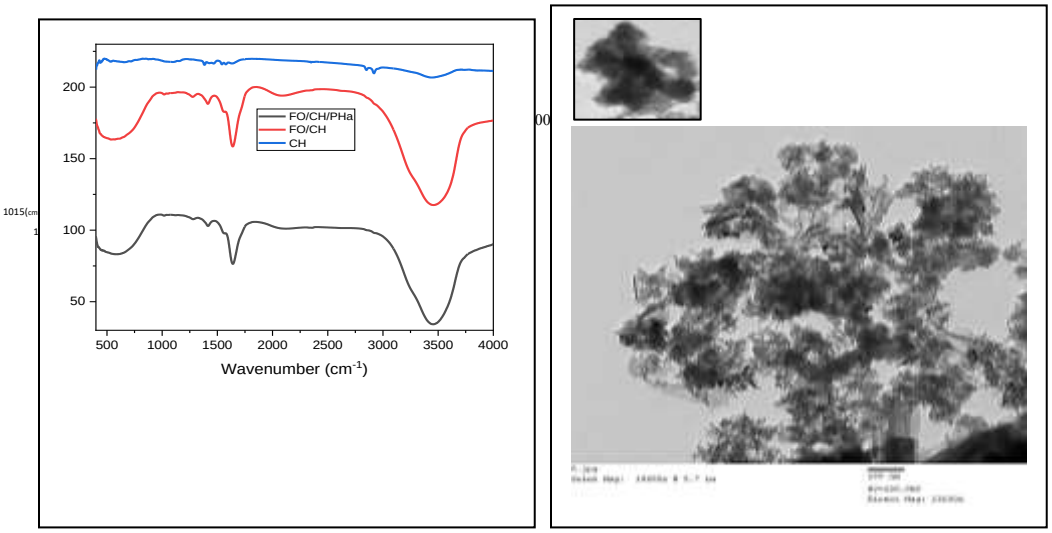

Figure 1: (a) FTIR analysis of CH, FO-CH, and Pha@FO-CH, (b) TEM image(600dpiviaimageJ) of Pha@FO-CH.

Upon comparing the FO-CH spectrum with the CH spectrum, a new IR absorption band at 1560 cm^{-1} was detected, indicating the presence of an amide bond in the FO-CH [35]. The presence of folic acid in the FO/CH was confirmed by the emergence of the C-N stretching bands in the 1015 cm^{-1} and 1279 cm^{-1} regions [36]. The peak observed at 1637 cm^{-1} corresponds to the stretching vibration of the iminic (-C=N-) bond [37]. There is a slight reduction in peak intensity of Pha@FO-CH NC compared to FO-CH, which can be attributed to the inhibition of vibrations or rotational modes within the Pha@FO-CH NC. The Pha@FO-CH NC alters the penetration depth and limits specific vibrational modes, leading to a decrease in intensity. The TEM image in Fig. 1 (b) reveals

that CH NPs are mainly spherical (as shown in the top left corner), with sizes ranging from 20 to 30 nm. This NPs size range exhibits enhanced physicochemical properties and can potentially improve their bioavailability and cellular uptake [38].
The UV-Vis spectrum provides valuable information about the chemical structure, electronic properties, and potential applications of compounds in various fields, such as pharmaceutical applications. The UV-Vis absorption spectrum of pheophorbide-a (Fig. 2-a) typically shows peaks at 409 nm and 663 nm. These peaks indicate the molecule's ability to absorb light at those specific wavelengths. The peak at 409 nm corresponds to the Soret band, which is associated with the π-π* electronic transitions of the porphyrin ring system. The peak at 663 nm corresponds to the Q-band, which is attributed to the metal-ligand charge transfer transitions [39]. Folic acid shows absorption peaks at around 280 nm and 370 nm due to its conjugated structure. The absorption at 280 nm is linked to aromatic amino acids like phenylalanine and tyrosine in folic acid. The absorption peak at 370 nm is associated with electronic transitions within the pteridine ring of folic acid. These absorption peaks can be attributed to the electronic transitions within the folic acid molecule. The absorption at 280 nm is associated with the π-π* transitions of the aromatic rings, while the absorption at 370 nm is related to the conjugated system within the pteridine ring of folic acid [40]. The UV-Vis spectrum of a conjugate of folic acid and pheophorbide-a exhibits a combination of absorption peaks from both compounds. The absorption at 284 nm, which is close to the absorption peak of folic acid, is attributed to the aromatic amino acids present in folic acid, such as phenylalanine and tyrosine. The weak absorption peak at 370 nm may correspond to the conjugation of the pteridine ring in the folic acid with the carboxyl group in Pha, in addition to broadening and red shift of the Soret band at 410 nm and Q-band at 664 nm of Pha. Overall, the UV-Vis spectrum of the folic acid/pheophorbide-a conjugate displays absorption bands, reflecting the combined characteristics of folic acid and pheophorbide-a in the conjugated form. High-performance liquid chromatography (HPLC) has also been used to separate and identify the organic components of the prepared NC [41]. HPLC in Fig. 2(b) showed that the product Pha@CH-FO NC has separated into three components which elute at a flow rate of 2.28 minutes, 3.08 minutes, and 5.88 minutes, corresponding to CH, FO, and Pha respectively. The HPLC chromatogram of the reactants (CH, FO, or Pha) is illustrated in Fig S1 of the supplementary file.

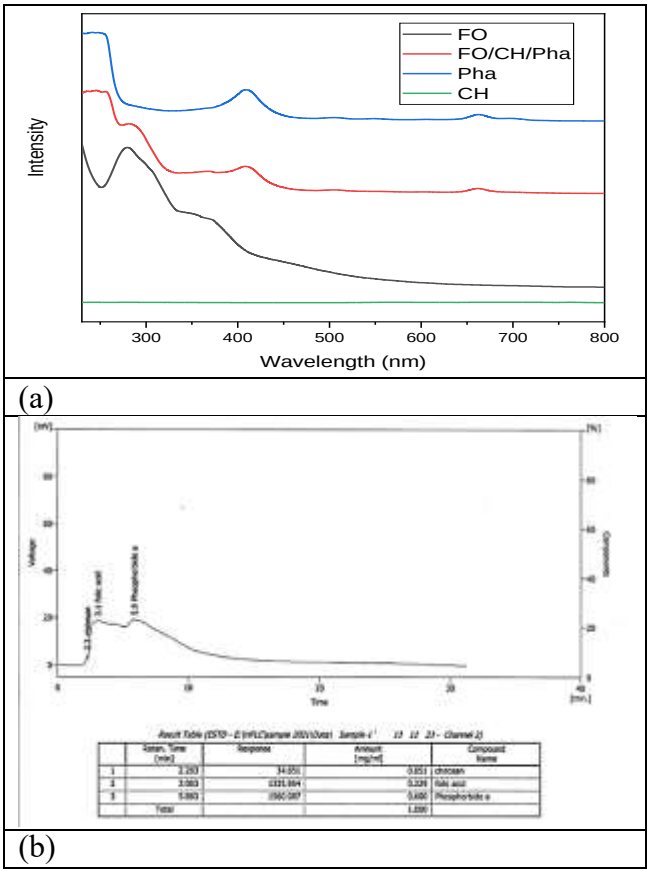

Figure 2: (a) UV-Vis absorption and (b) HPLC analysis of pha, CH, FO, and FO/CH/Pha,

Biological investigation

1. The cytotoxic effects of CH-FO and Pha@CH-FO NC on cell lines

Using the MTT assay, a cytotoxic screening was conducted for 24 hours (h) on MCF7, T-47D, MDA-MB-231, and HepG2 cell lines to determine the IC_{50} of CH-FO NC and Pha@CH-FO NC on each cell line. As shown in Fig. 3, Pha@CH-FO NC exhibited weak cytotoxicity on MDA-MB-231 and HepG2 cells after 24h while MCF-7 and T-47D cell lines showed IC_{50} values of 122.74 and 217.27 µg/mL, respectively. Previous studies reported that pure Pha demonstrated low cytotoxicity in dark conditions (Li et al. 2017). However, due to the CH-NPs also having an anti-cancer effect [28], the combined cell dark toxicity of the Pha and CH–NPs appeared at higher concentrations on MCF7 and T-47D cell lines. By the application of CH-FO, the IC50 was not reached (cytotoxicity was less than 50%) in all cell lines.

(a)

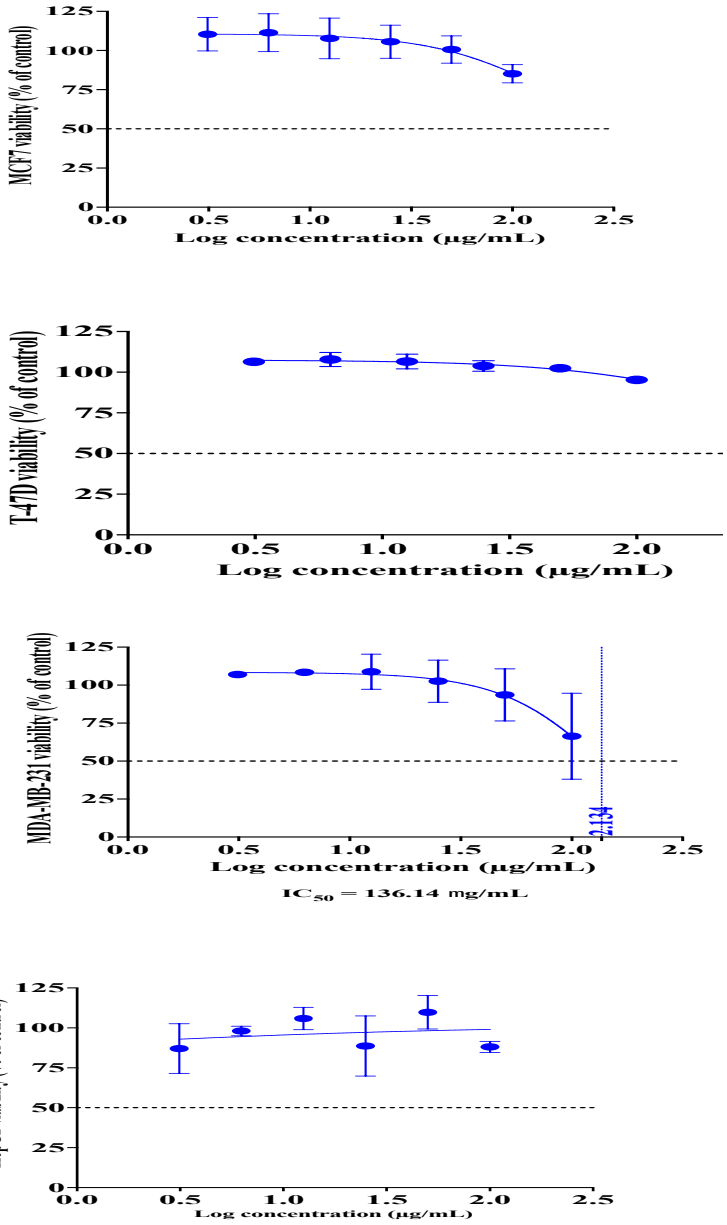

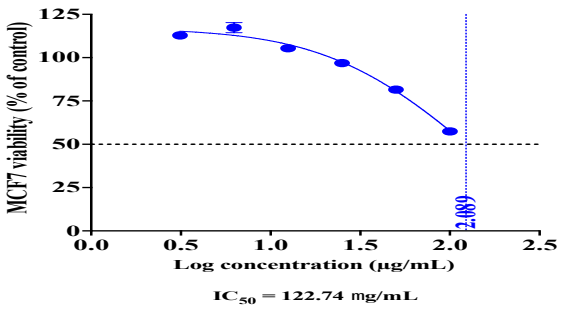

IC_{50} = 122.74 mg/mL

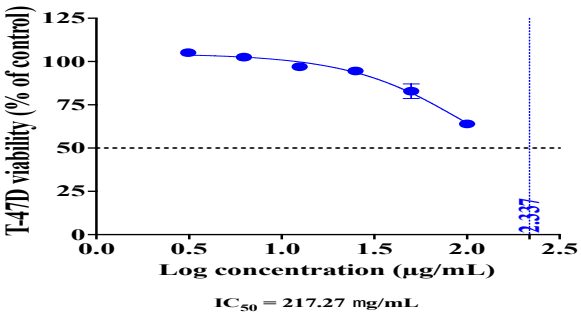

IC_{50} = 217.27 mg/mL

(b)

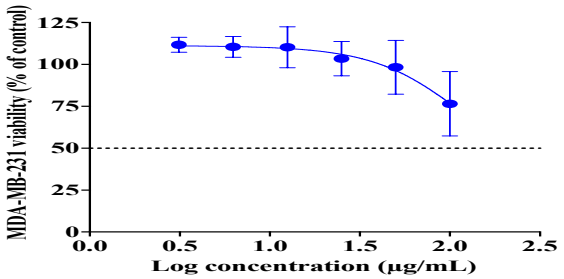

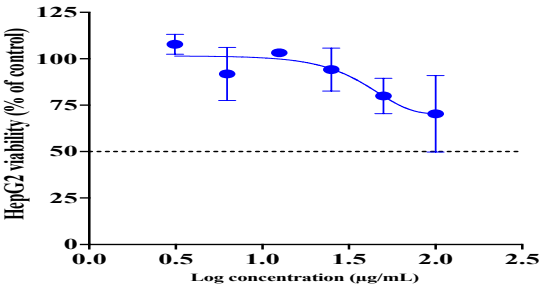

Figure 3: The dose response curve of CH-FO NC (a) and Pha@CH-FO NC (b) on MCF7, T-47D, MDA-MB-231, and HepG2 cell lines after 24h.

- The ½ IC_{50} was applied to the respective cell lines, and different laser conditions were applied to detect the most effective combination of Laser and tested samples. By application of Laser only, there was no considerable cytotoxic effect (less than 50% cytotoxicity) at all laser conditions in all cell lines as shown in **Fig. 4**(a), **5** (a), **6** (a), and **7** (a). This suggests that the Laser alone did not harm the cells significantly. Previous study on cultured mouse fibroblast cells disclosed that a blue laser (405 nm) led to a decline in cell viability due to a reduction in ATP levels in mouse skin cells and stimulated the production of superoxide anion and hypochlorous acid [42]. Also, applying Laser to CH-FO NC treated cells disclosed no enhanced cytotoxic effect (FIG S3, supplementary file). In contrast, applying different laser conditions to the Pha@CH-FO NC treated cells showed significant cytotoxicity in all cell lines. In the MCF7 cell line, the optimum laser conditions which result in 50% cytotoxicity, were 50 mW/96 seconds and 10 mW/500 seconds as shown in **Fig. 4** (b). On the T-47D cell line, the optimum laser conditions resulting in 50% cytotoxicity were 50 mW/96 seconds, 25 mW/400 seconds, and 10 mW/500 seconds as shown in **Fig. 5** (b). The MDA-MB-231 cell line was highly affected at 50 mW/200 seconds, 25 mW/ 400 seconds, and 10 mW/500 seconds, as shown in **Fig. 6** (b). The 50 mW/96 seconds, and 25 mW/400 seconds caused >50% cytotoxicity on the HepG2 cell line. Only the 10 mW/500 seconds laser irradiation caused almost 50% cytotoxicity, as shown in **Fig. 7** (b). This figure suggests that the combination of FO, CH NPs, and Pha led to cancer cells damage in conjunction with specific laser conditions. Due to the heterogeneity of tumors, consisting of diverse cell populations with varying sensitivities, longer laser exposure times may target resistant subpopulations.

(a)

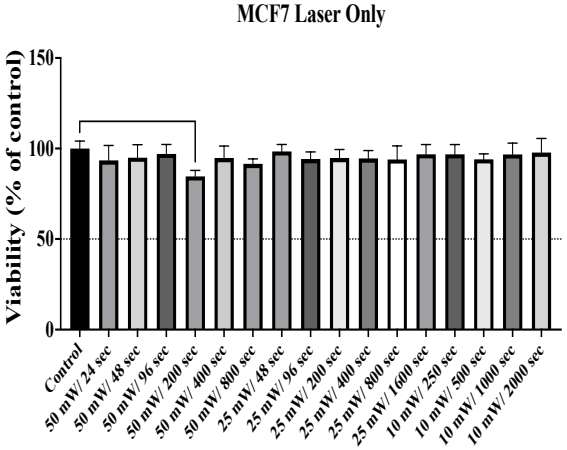

(b)

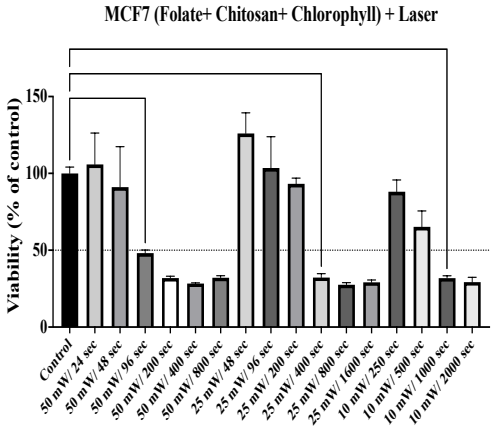

Figure 4: The cytotoxicity on MCF7 cell line of Laser alone (a), and Folate+ Chitosan+ Chlorophyll+ Laser (b). There was a significant difference between the control and the 50 mW/200-second groups in the laser-only groups. The application of Laser on (Folate+Chitosan+Chlorophyll) caused significant cytotoxicity differences between the control group and the 50 mW/ 96 seconds, 25 mW/ 400 seconds, and 10 mW/ 1000 seconds. The data were represented as mean±SD. *** p< 0.001.

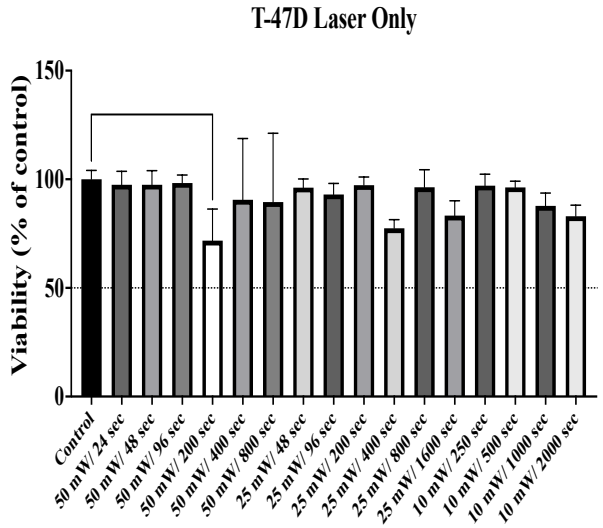

(a)

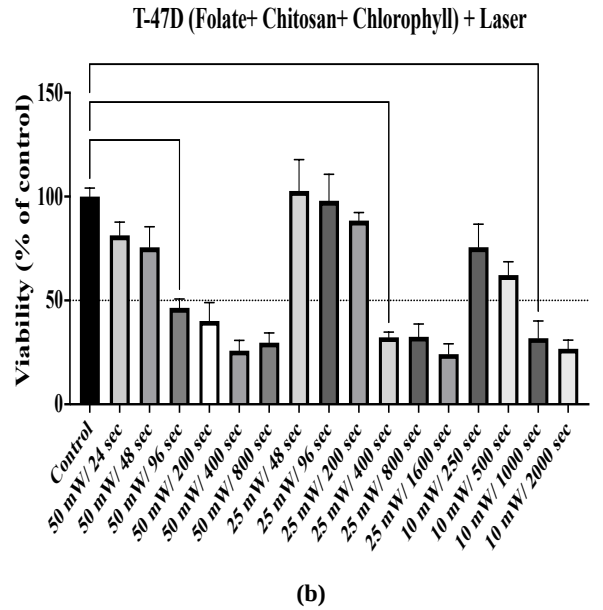

(b)

Figure 5: The cytotoxicity on T-47D cell line of Laser alone (a), Folate+ Chitosan+ Laser (b), and Folate+ Chitosan+ Chlorophyll+ Laser (c). Ordinary one-way ANOVA showed a significant difference between the control group and 50 mW/ 200 seconds when applying the Laser only. Applying a laser to (Folate+Chitosan) showed a significant difference between the control group and the 25 mW/ 96 seconds only. In the (Folate+ Chitosan+ Chlorophyll) + Laser study, cytotoxicity significantly differed between the control group and the 50 mW/96 seconds, 25 mW/ 400 seconds, and 10 mW/ 1000 seconds. The data was represented as mean±SD, *** $p < 0.001$.

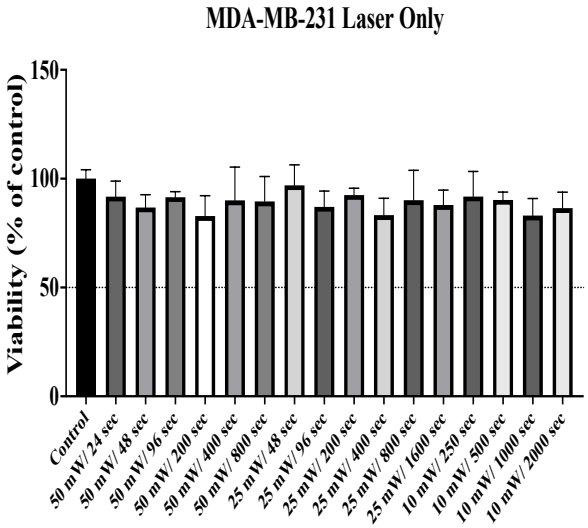

(a)

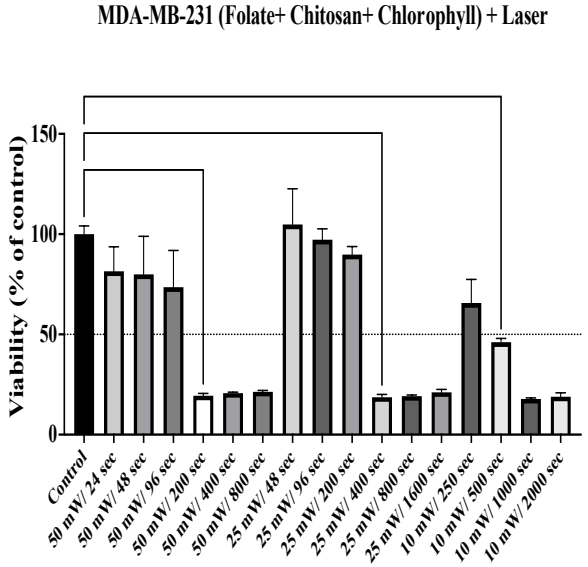

(b)

Figure 6: The cytotoxicity on MDA-MB-231 cell line of Laser alone (a), Folate+ Chitosan+ Laser (b), and Folate+ Chitosan+ Chlorophyll+ Laser (c). The Laser alone didn't exceed 25% cytotoxicity. Using Ordinary One-Way ANOVA, there was significant cytotoxicity between the control cells and the 50 mW/ 200 seconds and 10 mW/ 1000 seconds only. On applying Laser to (Folate+ Chitosan+ Chlorophyll), there was a significant difference between the control group and 50 mW/ 200 seconds, 25 mW/ 400 seconds, and 10 mW/ 500 seconds. The data was represented as mean± SD. *** $p < 0.001$.

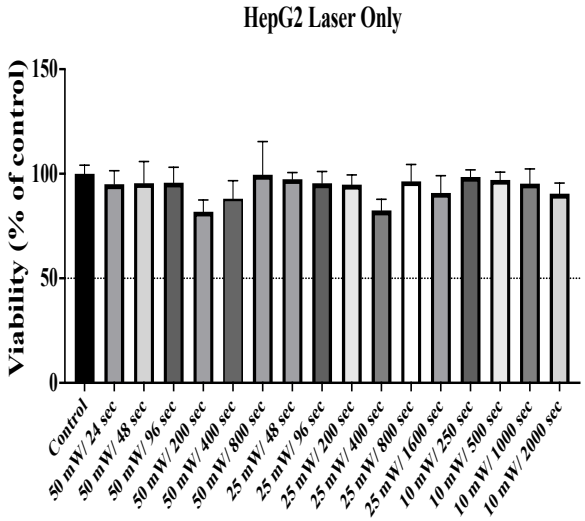

(a)

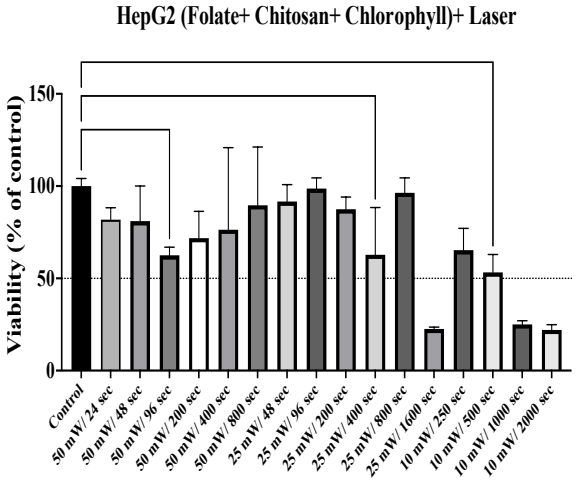

(b)

Figure 7: The cytotoxicity on HepG2 cell line of Laser alone (a) with no cytotoxicity effect reaching 25%, Folate+ Chitosan+ Laser (b), and Folate+ Chitosan+ Chlorophyll+ Laser (c). Using ordinary One-Way ANOVA in comparing (Folate+ Chitosan) + Laser (b), there was a significant difference between the control group, and there was a significant difference between the control group and 50 mW/ 96 hrs., 25 mW/ 400 seconds, and 10 mW/ 250 seconds. On applying Laser to (Folate+ Chitosan+ Chlorophyll), there was a significant difference between the control group and the 50 mW/96 seconds, 25 mW/400 seconds, and 10 mW/500 seconds, respectively. The data was represented as mean± SD, * $p< 0.05$, ** $p< 0.01$

- Here are some key findings related to PDT applying Pha. The mechanism of phototoxicity in HepG2 and HeLa cells revealed that Pba induces lipid peroxidation in cancer cells, as indicated by increased malonyldialdehyde and oxidized C11 BODIPY581/591 (lipid peroxidation sensor) [43]. Choi et al. 2014 illustrated that the transcription factor (NRF2), which protects against oxidative stress, can confer resistance to anti-cancer drugs. Knockdown of NRF2 in MDA-MB-231 cells and colon carcinoma HT29 cells enhances cytotoxicity, ROS levels, singlet oxygen production and PDT sensitivity. NRF2 knockdown reduces BCRP (breast cancer resistance protein) expression, leading to higher Pba accumulation and increased ROS, contributing

to enhanced cell death. The results show a considerable variation in phototoxicity among different cell lines**.** This may be due to differences in cellular pathways and responses. For example, **MDA-MB-231** cells may have higher expression of proteins involved in Pba uptake, localization, activation, or ROS generation, leading to increased phototoxicity. The balance between ROS production and antioxidant defense varies among cell lines. Some cell lines express detoxification enzymes (e.g., cytochrome P450) that can metabolize Pha, reducing its phototoxicity. **HepG2**, is known for its relatively high expression of antioxidant protection enzymes such as **Glutathione Peroxidase, Catalase, Superoxide Dismutase and NAD(P)H Quinone Oxidoreductase 1**. This Pba conjugate includes chitosan and folic acid, which enhances specificity. Folic acid binds to folate receptors overexpressed on cancer cells, allowing targeted delivery and minimize damage to healthy cells. Chitosan NPs may protect Pha by reducing systemic exposure and enhance its bioavailability [45]. In addition, the presence of chitosan in the form of NPs, facilitates Pha endocytosis by cells, plus its role in the antiangiogenic mechanism and inhibition of tumors [28].

2. The mode of cell death of the promising cytotoxic samples

Using the acridine orange/ ethidium bromide fluorescing stain (AO/EtBr), the different modes of cell death were investigated under the fluorescent microscope. Significant early apoptotic, late apoptotic, and necrotic changes were in all cells treated with Pha@CH-FO NC compared with control and laser-only irradiated cells. Mitochondrial chromophores absorb the laser energy at 405 nm. This absorption leads to the production of ROS. ROS can cause mitochondrial dysfunction, which activates apoptotic changes [46]. [47] Pha-PDT leads to early apoptotic changes of uterine carcinosarcoma due to the depolarization of mitochondrial membrane potential by rapidly generating singlet oxygen during light irradiation. This process occurs because Pha localizes in the mitochondria. As a result, cytochrome c is released, activating the intrinsic apoptotic pathway in cancer cells while in the late apoptotic changes, the cells exhibit features such as chromatin condensation, membrane blebbing, and shrinkage. Pha-PDT can also induce necrosis characterized by membrane rupture and loss of intracellular contents in cancer cells [48]. CH NPs can also induce cancer cells apoptosis by reducing glutathione and increasing ROS levels in cancer cells including leukemia [49]

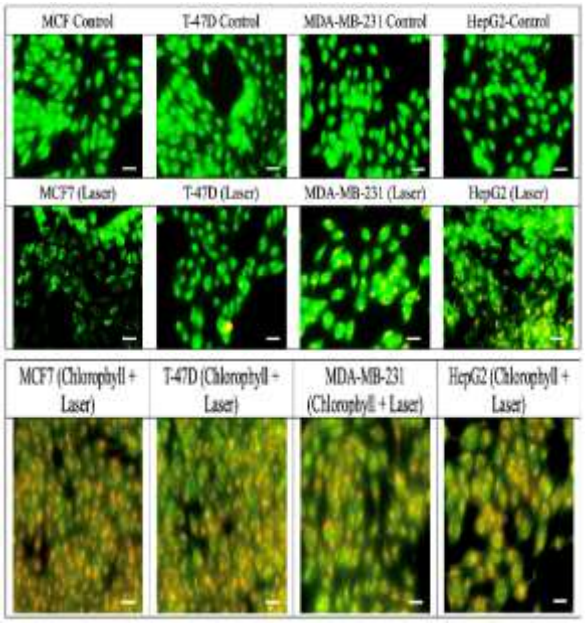

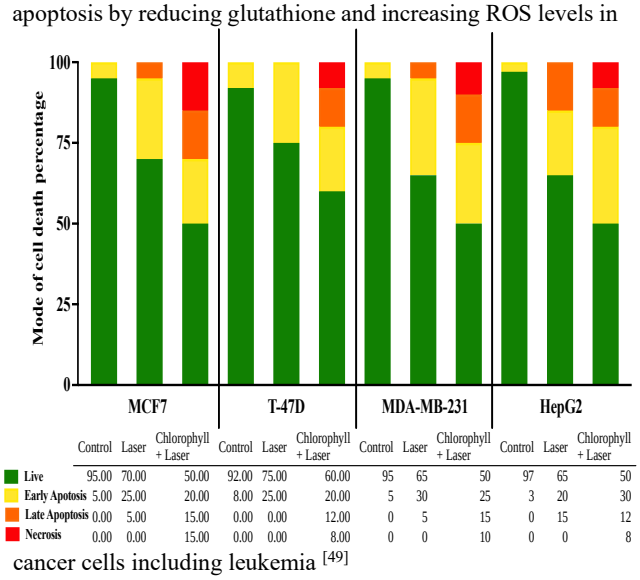

	MCF7			T-47D			MDA-MB-231			HepG2		
	Control	Laser	Chlorophyll + Laser	Control	Laser	Chlorophyll + Laser	Control	Laser	Chlorophyll + Laser	Control	Laser	Chlorophyll + Laser
Live	95.00	70.00	50.00	92.00	75.00	60.00	95	65	50	97	65	50
Early Apotosis	5.00	25.00	20.00	8.00	25.00	20.00	5	30	25	3	20	30
Late Apoptosis	0.00	5.00	15.00	0.00	0.00	12.00	0	5	15	0	15	12
Necrosis	0.00	0.00	15.00	0.00	0.00	8.00	0	0	10	0	0	8

Figure 8: The mode of cell death using fluorescence dye AO/EtBr in laser-only cells, (Folate+ Chitosan+ Chlorophyll) + Laser, compared to untreated control cells. a) . The fluorescent photos show live cells in the control cells, slight apoptotic changes in the laser-only group, and different stages of apoptosis and necrosis in the treated cells. b) the different modes of cell death distribution among all cell lines. The data shows increased early apoptotic changes together with late apoptosis. There were also valuable necrotic changes in all treated cells. The magnification is 20X. The scale bar is 50 µm

(a) **(b)**

3. The Bcl-2 protein expression

Bcl-2 protein family is an attractive target for cancer therapy. Using the immunofluorescence technique, the Bcl-2 protein expression was detected in each cell line after incubation with the Folate+ Chitosan+ Chlorophyll sample at the optimum laser conditions. There was a significant decrease ($p< 0.001$) in the protein expression in each treated sample compared to its untreated control. The protein expression is illustrated in **Fig. 9(a, b)**. The **Possible mechanism that may alter** Bcl-2 expression, including the generation of ROS by Pha after laser irradiation. This decrease in Bcl-2 expression promotes apoptosis in cancer cells [50].

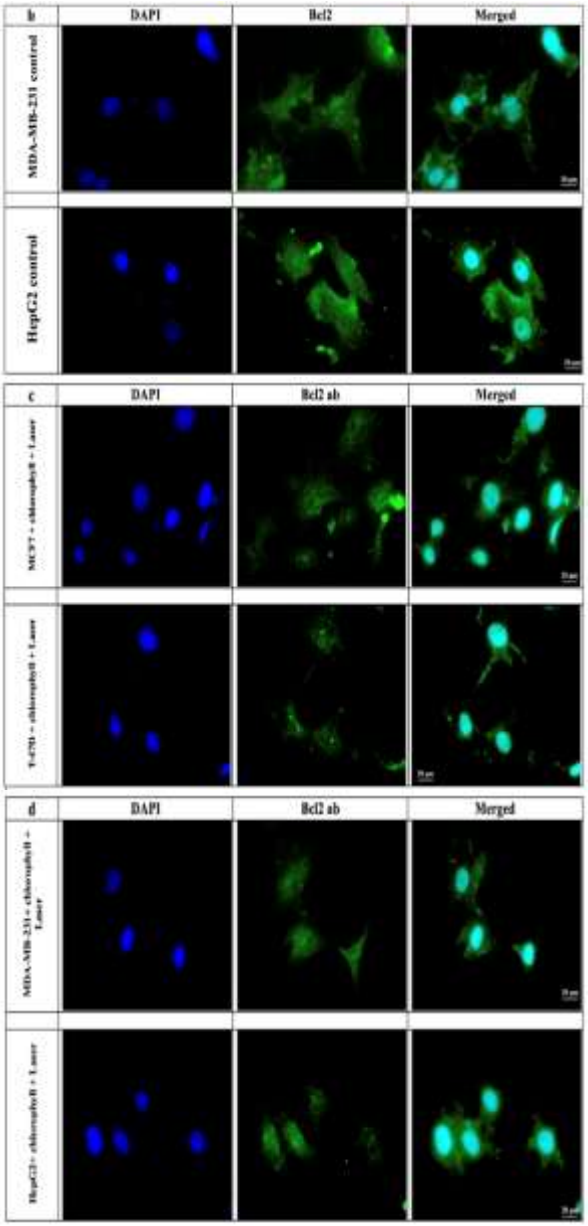

(a)

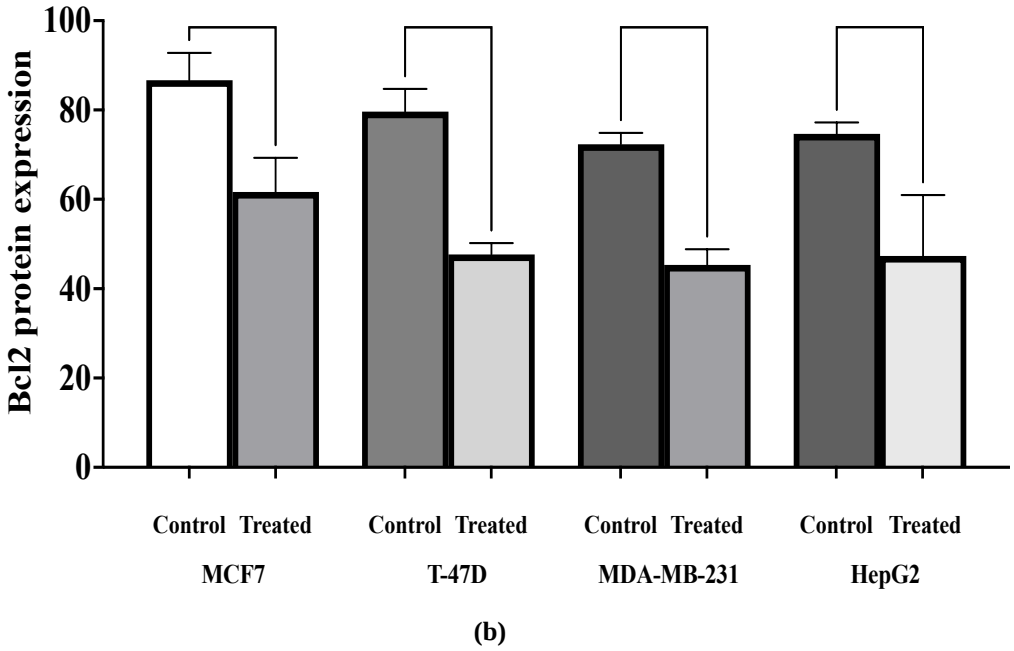

Figure 9: The Bcl2 protein expression using the immunofluorescence technique. a) the fluorescent photos of each cell line, the control cells show high expression of Bcl2 while the respective treated cells show a significant decrease in the protein expression. b) Ordinary One-Way ANOVA for the protein expression among control and treated cells. There is a significant decrease in the protein expression between the treated cells and its respective control cells. The data is represented as mean± SD. *** p< 0.001. The scale bar is 20 µm, the magnification is 40X. The data is based on 1000 cells.

4. The ROS detection

The ROS were quantified in each cell line using the fluorescent ROS detector kit at the optimum laser conditions and the respective ½ IC_{50} of Pha@CH-FO NC-treated sample. There was a significant increase in the ROS fluorescent intensity in the laser-treated samples in each cell line compared to the negative control cells. The dat a is illustrated in **Fig. 10 (a, b, c, and d)**. As discussed earlier, the laser energy is absorbed by mitochondrial chromophores, which produces OS [46]. In addition to depolarizing mitochondrial membrane potential by rapidly generating singlet oxygen during Pha light irradiation [47].

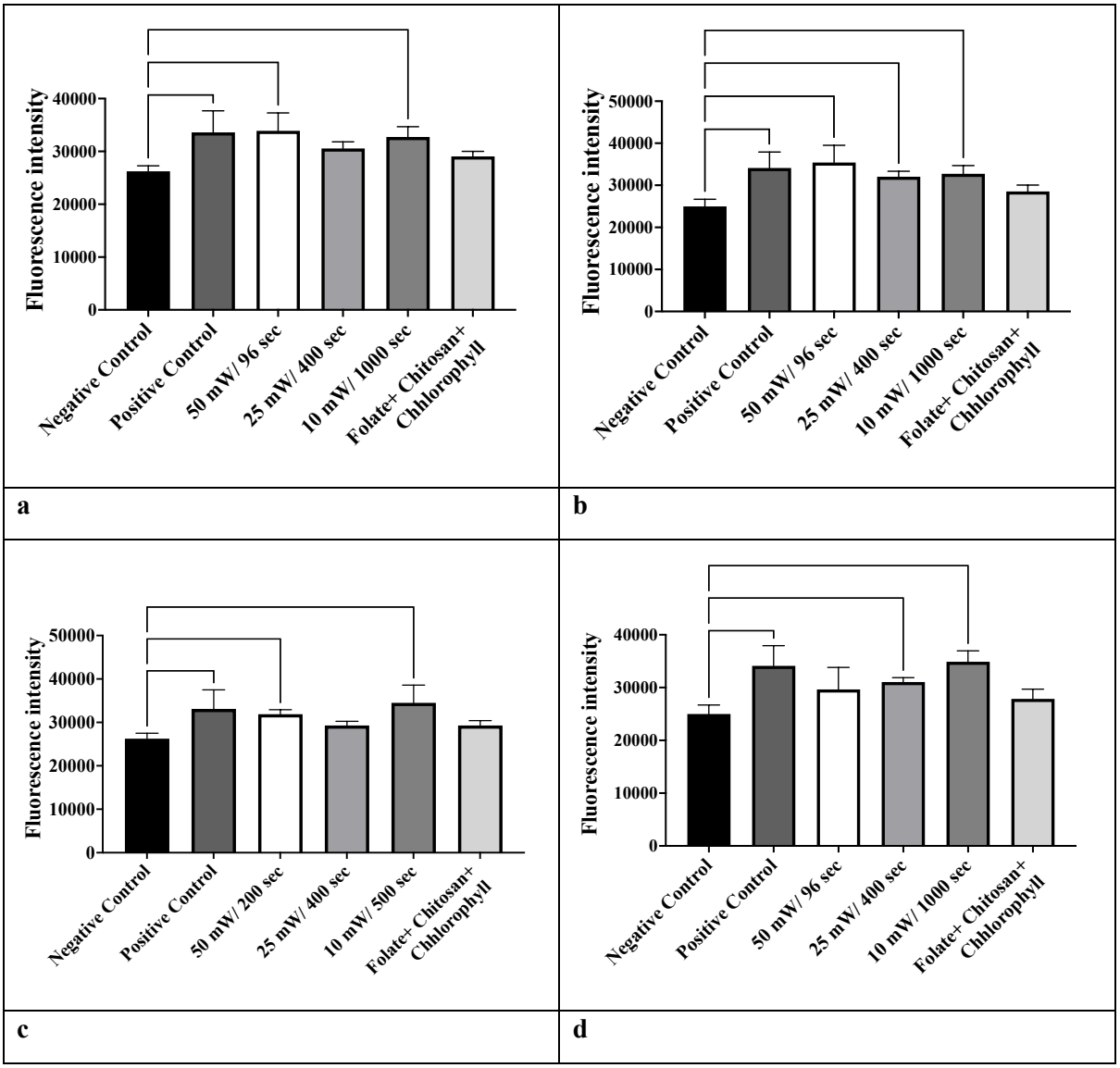

Figure 10: The ROS detection at different laser conditions in each cell line. a) In the MCF7 cell line, there is a significant increase in the ROS fluorescent intensity in the 50 mW/ 96 seconds and 10 mW/ 1000 seconds compared to the negative control cells. b) T-47D cell line, there is a significant increase in the ROS intensity in the 50 mW/ 96 seconds, 25 mW/ 400 seconds, and 10 mW/1000 seconds compared to the negative control cells. c) In the MDA-MB-231 cell line, there is a significant increase in the ROS fluorescent intensity in the 50 mW/ 200 seconds and 10 mW/ 500 seconds compared to the negative control cells. d) The HepG2 cell line shows a significant increase in the ROS fluorescent intensity in the 25 mW/ 400 seconds and 10 mW/ 1000 seconds compared to the negative control cells. The data is represented as mean± SD, * $p< 0.05$, ** $p< 0.01$, *** $p< 0.001$. n=4.

Conclusion

Inspired by successes in AuNRs-PTT, this study establishes Pha@CH-FO NC as a promising PDT agent, achieving targeted ROS-mediated apoptosis (Bcl-2 reduction: 60–70%) without thermal collateral damage. The NPs were characterized using FTIR analysis, TEM imaging, and UV-Vis spectroscopy. FTIR analysis revealed the presence of functional groups and chemical bonding within the composite material. TEM imaging showed that the chitosan NPs were mainly spherical and had sizes ranging from 20 to 30 nm. UV-Vis spectroscopy provided valuable information about the compounds' chemical structure and electronic properties. The cytotoxic effects of the samples on cancer cell lines were evaluated using the MTT assay, and it was found that the Pha@CH-FO NC exhibited weak dark cytotoxicity. Laser irradiation was applied to the samples, and significant cytotoxicity was observed in all cell lines when combined with the Pha@CH-FO NC. The different modes of cell death were investigated using fluorescence staining, and significant apoptotic and necrotic changes were observed in the treated cells. Bcl-2 protein expression was decreased in the treated cells compared to the control cells. ROS were detected and showed a significant increase in intensity in the laser-treated samples. Overall, this study demonstrated the potential cytotoxic effects of the Pha@CH-FO NC in cancer cells when combined with laser irradiation, along with an understanding of the underlying molecular mechanisms. These findings provide valuable insights into the development of intelligent nanostructures for more effective cancer treatment strategies, highlighting a need for continued research to exploit these therapeutic avenues in vivo. Future work will explore combinatorial PDT/PTT regimens, leveraging chitosan's versatility and AuNRs' photothermal efficiency to overcome tumor resistance mechanisms.

Declarations

Ethical Approval

This work does not apply to both human and/or animal studies.

Competing interests

I declare that the authors have no competing interests that might be perceived to influence the results and/or discussion reported in this paper.

Conflicts of Interest

The authors declare no conflict of interest.

Authors' contributions

All authors have contributed equally to the manuscript.

Funding

This research received funding from the Science, Technology & Innovation Funding Authority (STDF) under grant number 45893.

Acknowledgment

This paper is based upon work supported by the Science, Technology & Innovation Funding Authority (STDF) under grant number 45893.

References

[1] Gamal, H.; Tawfik, W.; El-Sayyad, H. I.; Emam, A. N.; Fahmy, H. M.; El-Ghaweet, H. A. A New Vision of Photothermal Therapy Assisted with Gold Nanorods for the Treatment of Mammary Cancers in Adult Female Rats. *Nanoscale Adv*, **2023**, *6* (1), 170–187. https://doi.org/10.1039/D3NA00595J.

[2] Gamal, H.; Tawfik, W.; El-Sayyad, H. H.; Fahmy, H. M.; Emam, A. N.; El-Ghaweet, H. A. Efficacy of Polyvinylpyrrolidone-Capped Gold Nanorods against 7, 12 Dimethylbenz (a) Anthracene-Induced Oviduct and Endometrial Cancers in Albino Rats. *Egyptian Journal of Basic and Applied Sciences*, **2023**, *10* (1).

[3] Gamal, H.; Tawfik, W.; Fahmy, H. M.; El-Sayyad, H. H. Breakthroughs of Using Photodynamic Therapy and Gold Nanoparticles in Cancer Treatment. *IEEE International Conference on Nanoelectronics, Nanophotonics, Nanomaterials, Nanobioscience & Nanotechnology (5NANO). IEEE.*, **2021**.

[4] Rapozzi, V.; Miculan, M.; Xodo, L. E. Evidence That Photoactivated Pheophorbide a Causes in Human Cancer Cells a Photodynamic Effect Involving Lipid Peroxidation. *Cancer Biol Ther*, **2009**, *8* (14), 1318–1327. https://doi.org/10.4161/CBT.8.14.8628.

[5] Tang, P. M. K.; Liu, X. Z.; Zhang, D. M.; Fong, W. P.; Fung, K. P. Pheophorbide a Based Photodynamic Therapy Induces Apoptosis via Mitochondrial-Mediated Pathway in Human Uterine Carcinosarcoma. *Cancer Biol Ther*, **2009**, *8* (6), 533–539. https://doi.org/10.4161/CBT.8.6.7694.

[6] Kaloni, D.; Diepstraten, S. T.; Strasser, A.; Kelly, G. L. BCL-2 Protein Family: Attractive Targets for Cancer Therapy. *Apoptosis*, **2023**, *28* (1–2), 20–38. https://doi.org/10.1007/S10495-022-01780-7.

[7] Leite, M.; Quinta-Costa, M.; Leite, P. S.; Guimarães, J. E. Critical Evaluation of Techniques to Detect and Measure Cell Death--Study in a Model of UV Radiation of the Leukaemic Cell Line HL60. *Anal Cell Pathol*, **1999**, *19* (3–4), 139–151. https://doi.org/10.1155/1999/176515.

[8] Li, W.; Tan, G.; Zhang, H.; Wang, Z.; Jin, Y. Folate Chitosan Conjugated Doxorubicin and Pyropheophorbide Acid Nanoparticles (FCDP–NPs) for Enhance Photodynamic Therapy. *RSC Adv*, **2017**, *7* (70), 44426–44437. https://doi.org/10.1039/C7RA08757H.

[9] El-ghannam, G.; Moawad, M.; Abo-Elfadl, M. T.; Elfeky, S. A. Beetroot Extract@chitosan Nanocomposite as a Promising Approach towards Cancer Therapy. *Int J Biol Macromol*, **2024**, *261* (Pt 1). https://doi.org/10.1016/J.IJBIOMAC.2024.129700.

[10] Ebrahimnejad, P.; Sodagar Taleghani, A.; Asare-Addo, K.; Nokhodchi, A. An Updated Review of Folate-Functionalized Nanocarriers: A Promising Ligand in Cancer. *Drug Discov Today*, **2022**, *27* (2), 471–489. https://doi.org/10.1016/J.DRUDIS.2021.11.011.

[11] Duthie, S. J. Folate and Cancer: How DNA Damage, Repair and Methylation Impact on Colon Carcinogenesis. *J Inherit Metab Dis*, **2011**, *34* (1), 101–109. https://doi.org/10.1007/s10545-010-9128-0.

[12] Wang, H.; Fan, Q.; Zhang, L.; Shi, D.; Wang, H.; Wang, S.; Bian, B. Folate-Targeted PTEN/AKT/P53 Signaling Pathway Promotes Apoptosis in Breast Cancer Cells. *Pteridines*, **2020**, *31* (1), 158–164. https://doi.org/10.1515/pteridines-2020-0020.

[13] Lu, Y. Folate Receptor-Targeted Immunotherapy of Cancer: Mechanism and Therapeutic Potential. *Adv Drug Deliv Rev*, **2004**, *56* (8), 1161–1176. https://doi.org/10.1016/j.addr.2004.01.009.

[14] Stiel, H.; Marlowb, I.; Roederb, B. *Photophysical Properties of the Photosensitizer Pheophorbide Studied at High Photon Flux Densities*; 1993; Vol. 17.

[15] Hoi, S. W.; Wong, H. M.; Chan, J. Y.; Yue, G. G. L.; Tse, G. M.; Law, B. K.; Fong, W. P.; Fung, K. P. Photodynamic Therapy of Pheophorbide a Inhibits the Proliferation of Human Breast Tumour via Both Caspase-dependent and -independent Apoptotic Pathways in *In Vitro* and *In Vivo* Models. *Phytotherapy Research*, **2012**, *26* (5), 734–742. https://doi.org/10.1002/ptr.3607.

[16] Tian, Y. Y.; Hu, X. Y.; Leung, W. N.; Yuan, H. Q.; Zhang, L. Y.; Cui, F. A.; Tian, X. Investigation of Photodynamic Effect Caused by MPPa-PDT on Breast Cancer. *Laser Phys Lett*, **2012**, *9* (10), 754–758. https://doi.org/10.7452/lapl.201210077.

[17] Komiyama, M.; Kobayashi, M.; Harada, M. Pheophorbide as Efficient Sensitizer for DNA Photocleavage. An Implication to Its Role in Photodynamic Cancer Therapy. *Chem Lett*, **1991**, *20* (12), 2123–2126. https://doi.org/10.1246/cl.1991.2123.

[18] Wang, K.-K.; Li, J.; Kim, B.-J.; Lee, J.-H.; Shin, H.-W.; Ko, S.-H.; Lee, W.-Y.; Lee, C.-H.; Jung, S. H.; Kim, Y.-R. Photophysical Properties of Pheophorbide-a Derivatives and Their Photodynamic Therapeutic Effects on a Tumor Cell Line *In Vitro*. *International Journal of Photoenergy*, **2014**, *2014*, 1–7. https://doi.org/10.1155/2014/793723.

[19] Sahu, S. K.; Mallick, S. K.; Santra, S.; Maiti, T. K.; Ghosh, S. K.; Pramanik, P. In Vitro Evaluation of Folic Acid Modified Carboxymethyl Chitosan Nanoparticles Loaded with Doxorubicin for Targeted Delivery. *J Mater Sci Mater Med*, **2010**, *21* (5), 1587–1597. https://doi.org/10.1007/s10856-010-3998-4.

[20] Wu, B.; Zhao, N. A Targeted Nanoprobe Based on Carbon Nanotubes-Natural Biopolymer Chitosan Composites. *Nanomaterials*, **2016**, *6* (11), 216. https://doi.org/10.3390/nano6110216.

[21] Aibani, N.; Rai, R.; Patel, P.; Cuddihy, G.; Wasan, E. K. Chitosan Nanoparticles at the Biological Interface: Implications for Drug Delivery. *Pharmaceutics*, **2021**, *13* (10), 1686. https://doi.org/10.3390/pharmaceutics13101686.

[22] AAT Bioquest team. Acetate Buffer (0.1 M, pH 5.0) Preparation and Recipe | AAT Bioquest https://www.aatbio.com/resources/buffer-preparations-and-recipes/acetate-buffer-ph-5 (accessed Nov 17, 2023).

[23] Li, W.; Tan, G.; Zhang, H.; Wang, Z.; Jin, Y. Folate Chitosan Conjugated Doxorubicin and Pyropheophorbide Acid Nanoparticles (FCDP–NPs) for Enhance Photodynamic Therapy. *RSC Adv.*, **2017**, *7* (70), 44426–44437. https://doi.org/10.1039/C7RA08757H.

[24] Li, W.; Tan, G.; Zhang, H.; Wang, Z.; Jin, Y. Folate Chitosan Conjugated Doxorubicin and Pyropheophorbide Acid Nanoparticles (FCDP–NPs) for Enhance Photodynamic Therapy. *RSC Adv*, **2017**, *7* (70), 44426–44437. https://doi.org/10.1039/C7RA08757H.

[25] Silva, C. L.; Perestrelo, R.; Silva, P.; Tomás, H.; Câmara, J. S. Volatile Metabolomic Signature of Human Breast Cancer Cell Lines. *Sci Rep*, **2017**, *7* (1), 43969. https://doi.org/10.1038/srep43969.

[26] Hansen, M. B.; Nielsen, S. E.; Berg, K. Re-Examination and Further Development of a Precise and Rapid Dye Method for Measuring Cell Growth/Cell Kill. *J Immunol Methods*, **1989**, *119* (2), 203–210. https://doi.org/10.1016/0022-1759(89)90397-9.

[27] Buranaamnuay, K. The MTT Assay Application to Measure the Viability of Spermatozoa: A Variety of the Assay Protocols. *Open Vet J*, **2021**, *11* (2), 251. https://doi.org/10.5455/OVJ.2021.v11.i2.9.

[28] El-ghannam, G.; Moawad, M.; Abo-Elfadl, M. T.; Elfeky, S. A. Beetroot Extract@chitosan Nanocomposite as a Promising Approach towards Cancer Therapy. *Int J Biol Macromol*, **2024**, *261*, 129700. https://doi.org/10.1016/j.ijbiomac.2024.129700.

[29] Leite, M.; Quinta-Costa, M.; Leite, P. S.; Guimarães, J. E. Critical Evaluation of Techniques to Detect and Measure Cell Death – Study in a Model of UV Radiation of the Leukaemic Cell Line HL60. *Analytical Cellular Pathology*, **1999**, *19* (3–4), 139–151. https://doi.org/10.1155/1999/176515.

[30] Wang, X.-W. Presence of Fas and Bcl-2 Proteins in BEL-7404 Human Hepatoma Cells. *World J Gastroenterol*, **1998**, *4* (6), 540. https://doi.org/10.3748/wjg.v4.i6.540.

[31] Terasaki, A.; Kurokawa, H.; Ito, H.; Komatsu, Y.; Matano, D.; Terasaki, M.; Bando, H.; Hara, H.; Matsui, H. Elevated Production of Mitochondrial Reactive Oxygen Species via Hyperthermia Enhanced Cytotoxic Effect of Doxorubicin in Human Breast Cancer Cell Lines MDA-MB-453 and MCF-7. *Int J Mol Sci*, **2020**, *21* (24), 9522. https://doi.org/10.3390/ijms21249522.

[32] Mohamed, K.; Mousa, S.; El-Bassyouni, G.; Abd El-Hady, B.; Tolba, E. Fabrication of Hydroxyapatite–Aluminum Silicate/Chitosan-Gelatin Biocomposites with In-Vitro Application by Preosteoblast Cells (MC3T3-E1). *Egypt J Chem*, **2022**, *0* (0), 0–0. https://doi.org/10.21608/ejchem.2022.102394.4791.

[33] Tajuddin Hafizi; Mehrnoosh Hasan Shahriari; Majid Abdouss; Shafiq Ahmad Kahdestani. Synthesis And Characterization of Vancomycin-Loaded Chitosan Nanoparticles For Drug Delivery.

[34] Chatterjee, S.; Salaün, F.; Campagne, C. The Influence of 1-Butanol and Trisodium Citrate Ion on Morphology and Chemical Properties of Chitosan-Based Microcapsules during Rigidification by Alkali Treatment. *Mar Drugs*, **2014**, *12* (12), 5801–5816. https://doi.org/10.3390/md12125801.

[35] Kumbhar, S. T.; Patil, R. Y.; Bhatia, M. S.; Choudhari, P. B.; Gaikwad, V. L. Synthesis and Characterization of Chitosan Nanoparticles Decorated with Folate and Loaded with Dasatinib for Targeting Folate Receptors in Cancer Cells. *OpenNano*, **2022**, *7*, 100043. https://doi.org/10.1016/j.onano.2022.100043.

[36] Rezaei, T.; Rezaei, M.; Karimifard, S.; Mahmoudi Beram, F.; Dakkali, M. S.; Heydari, M.; Afshari-Behbahanizadeh, S.; Mostafavi, E.; Bokov, D. O.; Ansari, M. J.; et al. Folic Acid-Decorated PH-Responsive Nanoniosomes With Enhanced Endocytosis for Breast Cancer Therapy: In Vitro Studies. *Front Pharmacol*, **2022**, *13*. https://doi.org/10.3389/fphar.2022.851242.

[37] San, H. H. M.; Alcantara, K. P.; Bulatao, B. P. I.; Sorasitthiyanukarn, F. N.; Nalinratana, N.; Suksamrarn, A.; Vajragupta, O.; Rojsitthisak, P.; Rojsitthisak, P. Folic Acid-Grafted Chitosan-Alginate Nanocapsules as Effective Targeted Nanocarriers for Delivery of Turmeric Oil for Breast Cancer Therapy. *Pharmaceutics*, **2022**, *15* (1), 110. https://doi.org/10.3390/pharmaceutics15010110.

[38] Gül, D.; Önal Acet, B.; Lu, Q.; Stauber, R. H.; Odabaşı, M.; Acet, Ö. Revolution in Cancer Treatment: How Are Intelligently Designed Nanostructures Changing the Game? *Int J Mol Sci*, **2024**, *25* (10), 5171. https://doi.org/10.3390/ijms25105171.

[39] Rapozzi, V.; Miculan, M.; Xodo, L. Evidence That Photoactivated Pheophorbide a Causes in Human Cancer Cells a Photodynamic Effect Involving Lipid Peroxidation. *Cancer Biol Ther*, **2009**, *8* (14), 1318–1327. https://doi.org/10.4161/cbt.8.14.8628.

[40] Nara, S.; Parasher, G.; Malhotra, B. D.; Rawat, M. Novel Role of Folate (Vitamin B9) Released by Fermenting Bacteria under Human Intestine like Environment. *Sci Rep*, **2023**, *13* (1), 20226. https://doi.org/10.1038/s41598-023-47243-0.

[41] Swartz, M. HPLC Detectors: A Brief Review. *J Liq Chromatogr Relat Technol*, **2010**, *33* (9–12), 1130–1150. https://doi.org/10.1080/10826076.2010.484356.

[42] Nakayama, E.; Kushibiki, T.; Mayumi, Y.; Azuma, R.; Ishihara, M.; Kiyosawa, T. Blue Laser Irradiation Decreases the ATP Level in Mouse Skin and Increases the Production of Superoxide Anion and Hypochlorous Acid in Mouse Fibroblasts. *Biology (Basel)*, **2022**, *11* (2), 301. https://doi.org/10.3390/biology11020301.

[43] Rapozzi, V.; Miculan, M.; Xodo, L. Evidence That Photoactivated Pheophorbide a Causes in Human Cancer Cells a Photodynamic Effect Involving Lipid Peroxidation. *Cancer Biol Ther*, **2009**, *8* (14), 1318–1327. https://doi.org/10.4161/cbt.8.14.8628.

[44] Choi, B.; Ryoo, I.; Kang, H. C.; Kwak, M.-K. The Sensitivity of Cancer Cells to Pheophorbide A-Based Photodynamic Therapy Is Enhanced by NRF2 Silencing. *PLoS One*, **2014**, *9* (9), e107158. https://doi.org/10.1371/journal.pone.0107158.

[45] Sharifi-Rad, J.; Quispe, C.; Butnariu, M.; Rotariu, L. S.; Sytar, O.; Sestito, S.; Rapposelli, S.; Akram, M.; Iqbal, M.; Krishna, A.; et al. Chitosan Nanoparticles as a Promising Tool in Nanomedicine with Particular Emphasis on Oncological Treatment. *Cancer Cell Int*, **2021**, *21* (1), 318. https://doi.org/10.1186/s12935-021-02025-4.

[46] da Silva, J. L.; Silva-de-Oliveira, A. F. S.; Andraus, R. A. C.; Maia, L. P. Effects of Low Level Laser Therapy in Cancer Cells—a Systematic Review of the Literature. *Lasers Med Sci*, **2020**, *35* (3), 523–529. https://doi.org/10.1007/s10103-019-02824-2.

[47] Tang, P. M.-K.; Liu, X.-Z.; Zhang, D.-M.; Fong, W.-P.; Fung, K.-P. Pheophorbide a Based Photodynamic Therapy Induces Apoptosis via Mitochondrial-Mediated Pathway in Human Uterine Carcinosarcoma. *Cancer Biol Ther*, **2009**, *8* (6), 533–539. https://doi.org/10.4161/cbt.8.6.7694.

[48] Rapozzi, V.; Miculan, M.; Xodo, L. Evidence That Photoactivated Pheophorbide a Causes in Human Cancer Cells a Photodynamic Effect Involving Lipid Peroxidation. *Cancer Biol Ther*, **2009**, *8* (14), 1318–1327. https://doi.org/10.4161/cbt.8.14.8628.

[49] Zivarpour, P.; Hallajzadeh, J.; Asemi, Z.; Sadoughi, F.; Sharifi, M. Chitosan as Possible Inhibitory Agents and Delivery Systems in Leukemia. *Cancer Cell Int*, **2021**, *21* (1), 544. https://doi.org/10.1186/s12935-021-02243-w.

[50] Kaloni, D.; Diepstraten, S. T.; Strasser, A.; Kelly, G. L. BCL-2 Protein Family: Attractive Targets for Cancer Therapy. *Apoptosis*, **2023**, *28* (1–2), 20–38. https://doi.org/10.1007/s10495-022-01780-7.